

$\bar{\nu}_\mu \leftrightarrow \bar{\nu}_e$  mixing: analysis of recent indications  
and implications for neutrino oscillation phenomenology

G. L. Fogli, E. Lisi, and G. Scioscia  
*Dipartimento di Fisica and Sezione INFN di Bari,  
Via Amendola 173, I-70126 Bari, Italy*

Abstract

We reanalyze the recent data from the Liquid Scintillator Neutrino Detector (LSND) experiment, that might indicate  $\bar{\nu}_\mu \leftrightarrow \bar{\nu}_e$  mixing. This indication is not completely excluded by the negative results of established accelerator and reactor neutrino oscillation searches. We quantify the region of compatibility by means of a thorough statistical analysis of all the available data, assuming both two-flavor and three-flavor neutrino oscillations. The implications for various theoretical scenarios and for future oscillation searches are studied. The relaxation of the LSND constraints under different assumptions in the statistical analysis is also investigated.

PACS number(s): 14.60.Pq, 14.60.Lm, 13.15.+g

## I. INTRODUCTION

The Liquid Scintillator Neutrino Detector (LSND) [1] collaboration at the Los Alamos Meson Physics Facility (LAMPF) claim evidence for neutrino oscillations  $\bar{\nu}_\mu \leftrightarrow \bar{\nu}_e$  from muon decay at rest [2,3], confirming preliminary results reported in [4].

The neutrino energy range,  $E_\nu \simeq 20\text{--}53$  MeV, and the path length,  $L \simeq 30$  m, make the LSND experiment particularly sensitive to neutrino mass differences in the eV range, which is of great interest for cosmological structure formation (see, e.g., [5]). Mass differences of the same order are probed by other accelerator and reactor neutrino oscillation experiments [6], which, however, do not find evidence for oscillations. Therefore, the interpretation of the LSND results as a neutrino oscillation effect requires careful checks and independent experimental confirmation. In the meanwhile, it is legitimate to study its possible implications in the phenomenology of neutrino masses and mixing.

The usual and easiest way to study the LSND signal is in terms of pure two-flavor oscillations. More precisely, the tau neutrino is assumed to be decoupled, so that only  $\nu_\mu \leftrightarrow \nu_e$  oscillations<sup>1</sup> may occur. The LSND oscillation signal can then be compared, in the usual mass-mixing plane, to the limits coming from experiments probing the same flavor appearance channel (E776 [7] and the Karlsruhe Rutherford Medium Energy Neutrino (KARMEN) experiment [8–10]), as well as those probing  $\nu_e$  disappearance (reactors Gösigen [11], Bugey [12], and Krasnoyarsk [13]) and  $\nu_\mu$  disappearance (CERN experiment CDHSW [14]). So far, this comparison has been simply performed by superposing the published 90% C.L. limits (see, e.g., Fig. 31 in [2]). However, the intersection of 90% C.L. regions *is not* a 90% C.L. region, and a more refined combination of the different experimental results is desirable.

A three-flavor oscillation framework is required if, in addition, one wants to study the interplay between LSND and the *tau* neutrino appearance experiments, such as E531 at Fermilab [15] (completed), the CERN Hybrid Oscillation Research Apparatus (CHORUS) [16], and the Neutrino Oscillation Magnetic Detector (NOMAD) experiment [17]. The most general three-flavor approach would imply a reanalysis of all the data in a huge parameter space. However, if two of the three neutrinos are assumed to be almost degenerate in mass (so that the oscillations are driven by just one mass parameter at the laboratory scale), then the three-flavor analysis becomes much more manageable (see [18,19] and references therein). Many authors [20–30] have recently compared the LSND results with previous laboratory neutrino oscillation data within such approximation. In all these analyses [20–30], the quoted limits on the neutrino masses and mixings were simply obtained as intersections of the region of parameter *preferred* by LSND and the regions *excluded* by the other oscillation experiments. As for the two-flavor case, no definite confidence level can be attached to such limits and to the corresponding scenarios, with the additional complication that the degrees of freedom increase when passing from a two-flavor to a three-flavor oscillation scheme.

Motivated by the wide interest in the LSND results, and by the lack of a rigorous com-

---

<sup>1</sup>In the following, neutrinos and antineutrinos will not be distinguished. Their oscillations in vacuum are equivalent both in the two-flavor limit and in the three-flavor scheme that we will use.

parison with the established accelerator and reactor neutrino oscillation limits, we set out to quantify this comparison in a statistically consistent approach. We build upon our previous work [18], in which the results of the most constraining negative searches for neutrino oscillations were reanalyzed *ab initio* and combined in a global  $\chi^2$  analysis. In the present work we include in the data set the recent LSND and KARMEN results, using both a two-flavor and a three-flavor approach. We obtain precise bounds on neutrino mixings and mass differences, in the hypothesis that the LSND signal can indeed be interpreted as evidence for neutrino oscillations. These bounds are then used to discuss various scenarios described in [20–30], as well as to investigate possible expectations for future laboratory oscillation searches. As a byproduct of our reanalysis of the LSND data, we gain interesting information on the stability of the neutrino oscillation fit. In particular, we show how the LSND constraints get weakened when the energy distribution of the LSND signal is gradually integrated out.

Our work is organized as follows. In Sec. II we combine the LSND results with all the other established accelerator and reactor data relevant for two-flavor oscillations  $\nu_\mu \leftrightarrow \nu_e$ , and derive bounds on the neutrino mass and mixing parameters. In Sec. III we include also the data from the established  $\nu_\tau$  appearance searches in a three-flavor oscillation framework with hierarchical mass differences. In Sec. IV we investigate the implications of our results on some phenomenological scenarios and on future oscillation searches. We draw our conclusions in Sec. V. Our reanalysis of the LSND data is presented in Appendix A, together with a critical investigation of the stability of the fit. The reanalysis of the KARMEN data is detailed in Appendix B.

## II. ANALYSIS IN TWO FLAVORS

Let us assume pure two-flavor oscillations between the electron and muon neutrino, with mass-mixing parameters  $(m^2, \sin^2 2\theta)$ . The event excess claimed by the LSND collaboration constrains these parameters in a relatively narrow region, as shown in Fig. 31 of [2].

We have independently reanalyzed the published LSND data with a maximum likelihood method, as detailed in Appendix A. The results are shown in Fig. 1. The 90 and 99 % C.L. contours compare well with the LSND confidence limits (Fig. 31 of [2]), except for a “wobble” at  $m^2 \simeq 3 \text{ eV}^2$  that, in our fit, extends to higher values of  $\sin^2 2\theta$ . This difference is irrelevant, being located in the region excluded by other established neutrino oscillation searches (as we shall see). Our best fit is reached for  $(m^2, \sin^2 2\theta) = (3 \text{ eV}^2, 0.009)$ . The best-fit point is not particularly important in itself, since good fits are also reached in other zones that form a set of almost-degenerate maxima of the likelihood function  $\mathcal{L}$ , as can be realized by looking at the 68% C.L. contours of Fig. 1. One of the local maxima practically coincides with the best-fit point of the published LSND analysis [2]  $(m^2, \sin^2 2\theta) = (19 \text{ eV}^2, 0.006)$ . The fit disfavors values of  $m^2$  close to integer multiples of  $4.3 \text{ eV}^2$ , for which the oscillation probability of the high-energy neutrinos (which are responsible for most of the event excess) is suppressed.

The reader is referred to Appendix A for an extensive discussion of the LSND data fit. Here we just anticipate that variations in the statistical treatment of the data may produce nonnegligible changes in the fit. In particular, the evidence in favor of neutrino oscillations appears to be weakened as the energy distribution of the LSND event excess

is gradually integrated. Therefore, we think that the exact shape of the present LSND confidence contours should be taken with a grain of salt, while waiting for higher statistics and more stable fits. For definiteness, however, we will always refer to the LSND limits as derived from our maximum likelihood reanalysis (Fig. 1) of the published LSND data. The combination with the data from other experiments is performed through the  $\chi^2$  method. To this purpose, the LSND likelihood is transformed as  $\chi^2 = -\ln \mathcal{L}/2$ ; the LSND  $\chi^2$  is then summed to the  $\chi^2$ 's of the other experiments.

The LSND indications can be directly compared with the (negative) results from two experiments that probed the same oscillation channel  $\nu_\mu \leftrightarrow \nu_e$ , namely KARMEN [9] and E776 [7]. Our reanalysis of the KARMEN data is described in detail in Appendix B. The results agree very well with the published oscillation bounds [9]. Figure 2(a) shows our estimated 90 and 99 % C.L. contours for the KARMEN experiment ( $\Delta\chi^2 = 4.61$  and 9.21 for two degrees of freedom).

Figure 2(b) shows the results of a combined fit to the LSND and KARMEN data. The regions allowed at 90 and 99 % C.L. are only slightly restricted with respect to Fig. 1, as most of the LSND oscillation signal is beyond the present KARMEN sensitivity. However, the KARMEN experiment should be able to test a significantly larger region of the parameter space in about two years [9].

The results from the E776 experiment [7] are more constraining than those from KARMEN. In Fig. 2(c) we report the E776 exclusion contours as derived by our reanalysis of the E776 data [18]. The combination with the LSND and KARMEN data is shown in Fig. 2(d). Notice that the 90% C.L. region of Fig. 2(d) is significantly larger than the intersection (not shown) of the 90% C.L. regions allowed by the LSND, KARMEN, and E776 experiments separately, especially for small mixing. The reason is that the E776 (and KARMEN) negative results are compatible with no mixing, and thus push the combined fit towards values of the mixing angle smaller than those allowed by LSND alone. Moreover, the addition of the E776 data weakens the global evidence for oscillations, so that the no oscillation limit is allowed at 99% C.L. in Fig. 2(d), while it is excluded in Fig. 2(b). In other words, by adding the E776 and KARMEN data, the gradient of the  $\chi^2$  is suppressed for small values of the oscillation parameters, so that the 90% C.L. constraints are significantly relaxed in that direction, and the 99% C.L. left contour disappears. These results show that a combined analysis of the neutrino oscillation data may give rather different bounds than the naive “superposition” of oscillation limits, especially when the individual experimental results pull the fit in different directions.

In the two-flavor approximation, the  $\nu_e$  disappearance searches at reactor experiments can be interpreted as probes of  $\nu_e \leftrightarrow \nu_\mu$  oscillations. The data from the Gösgen [11], Bugey [12], and Krasnoyarsk [13] experiments were reanalyzed and combined in [18]. The results are shown in Fig. 2(e). When combined with the LSND, KARMEN, and E776 data, the reactor results exclude the region at large mixing and low mass differences, as shown in Fig. 2(f). Notice that the narrow, disconnected regions allowed at 90% C.L. at large  $m^2$  in Fig. 2(f) would disappear if a simple superposition of oscillation plots were made instead of a global fit.

Finally, we mention that the results from  $\nu_\mu$  disappearance searches can also be added straightforwardly in the two-flavor approximation. However, the available data (CDHSW experiment [14]) probe relatively large mixing angles, and we have checked that their addition

produces negligible changes (not shown) to the contours of Fig. 2(f). The CDHSW data are anyway added, in the way described in [18], in the global three-flavor analysis of the following section.

### III. ANALYSIS IN THREE FLAVORS

In this section we combine with the  $\chi^2$  method the data from eight (reanalyzed) neutrino oscillation experiments (LSND, KARMEN, E776, Gösgen, Krasnoyarsk, Bugey, CDHSW, and E531 [31]), working in the simple three-flavor framework described in [18]. This framework is characterized by the assumption that two out of three neutrino mass eigenstates  $\nu_i$  ( $i = 1, 2, 3$ ) are effectively degenerate in mass,  $|m_2^2 - m_1^2| \simeq 0$ , while the mass gap of the “lone” state  $\nu_3$  is taken in the range of laboratory neutrino oscillation experiments:  $m^2 = |m_3^2 - m_{2,1}^2| \gtrsim 10^{-3} \text{ eV}^2$ . The neutrino oscillation parameter space is then spanned by three variables only: the dominant square mass difference  $m^2$ , and the mixing angles  $\phi$  and  $\psi$  (equal to  $\theta_{13}$  and  $\theta_{23}$  in the standard ordering of mixing matrices [6]). More precisely:

$$m^2 = |m_3^2 - m_{2,1}^2| \gg |m_2^2 - m_1^2| , \quad (1a)$$

$$\nu_3 = \sin \phi \nu_e + \cos \phi (\sin \psi \nu_\mu + \cos \psi \nu_\tau) , \quad (1b)$$

with  $\psi, \phi \in [0, \pi/2]$ . We prefer to use the variables  $(\tan^2 \psi, \tan^2 \phi)$ , which prove very useful for graphical representations [18]. Notice that the two-flavor oscillation limits  $\nu_\mu \leftrightarrow \nu_\tau$ ,  $\nu_e \leftrightarrow \nu_\tau$ , and  $\nu_e \leftrightarrow \nu_\mu$ , are reached for  $\phi = 0$ ,  $\psi = 0$ , and  $\psi = \pi/2$ , respectively. The reader is referred to [18] for further details and bibliography.

Figure 3 shows the results of our analysis in the  $(m^2, \tan^2 \phi)$  plane, for twelve representative values of  $\tan^2 \psi$ . The 90 and 99 % C.L. contours shown in each panel represent sections (at fixed  $\tan^2 \psi$ ) of the confidence volume defined by  $\chi^2 - \chi_{\min}^2 = 6.25$  and 11.36 respectively (for three degrees of freedom).

In the first panel of Fig. 3 the value of  $\tan^2 \psi$  is very large, corresponding to almost pure  $\nu_\mu \leftrightarrow \nu_e$  oscillations ( $\psi \rightarrow \pi/2$ ). In fact, the limits close to the left side of the first panel represent a mapping of the two-flavor oscillation limits shown in Fig. 2(f) (modulo the different number of degrees of freedom). The mirror limits on the right ( $\phi \rightarrow \pi/2 - \phi$ ) in the same panel come from enlarging the mixing angle range from  $[0, \pi/4]$  (2 flavors) to  $[0, \pi/2]$  (3 flavors or more).

In the subsequent panels the value of  $\tan^2 \psi$  gradually decreases and the mixing of  $\nu_3$  with  $\nu_\tau$  increases. The  $2\nu$  left-right symmetry of the plots ( $\phi \rightarrow \pi/2 - \phi$ ) is broken. The allowed regions get gradually shrunked, since for  $\psi \rightarrow 0$  one approaches the two-flavor oscillation limit  $\nu_e \leftrightarrow \nu_\tau$ , which is not compatible with the LSND data. The allowed regions on the left half of each panel disappear more rapidly, since for  $\psi \rightarrow 0$  and  $\phi \rightarrow 0$  the relevant mass eigenstate ( $\nu_3$ ) tends to become a flavor eigenstate ( $\nu_\tau$ ) and the oscillation phenomenon vanishes. Notice that the combination of all the data constrains  $m^2$  above  $\sim 0.2 \text{ eV}^2$  at 90% C.L. However, at 99% C.L. there is no lower bound on  $m^2$  and the global fit becomes compatible with no oscillations.

Figure 4 shows an alternative representation of the same confidence volume of Fig. 3. The volume is shown in  $(\tan^2 \psi, \tan^2 \phi)$  sections at fixed values of  $m^2$ . We remind that

the left, right, and lower side of each panel correspond, asymptotically, to pure  $\nu_e \leftrightarrow \nu_\tau$ ,  $\nu_e \leftrightarrow \nu_\mu$ , and  $\nu_\mu \leftrightarrow \nu_\tau$  oscillations, respectively. In Fig. 4, the region allowed at 90% C.L. generally consists of two disconnected parts at low and high  $\phi$ . These zones would be continuously connected by a C-shaped band if only the LSND data were fitted [18]. However, the data from all other oscillation experiments strongly disfavor the central part of each panel, corresponding to large (and not observed) three-flavor mixing. The width of the 90% allowed regions is very sensitive to small variations of  $m^2$  around multiples of 4.3 eV<sup>2</sup> where, as noticed, the LSND oscillation probability is suppressed. This is particularly evident in the panel at  $m^2 = 13$  eV<sup>2</sup> where no combination of mixing angles is allowed at 90% C.L. As in Fig. 3, the no oscillation scenario (corresponding to the lower corners and the upper side of each panel) appears to be allowed at 99% C.L. by the combination of all the data.

Figures 3 and 4 are the main result of this work. They represent a concise summary (in a three-flavor scheme) of the most constraining neutrino oscillation data available, in the hypothesis that the LSND signal can indeed be interpreted as a signal of neutrino oscillations.

#### IV. PHENOMENOLOGICAL IMPLICATIONS

In this section we study the implication of the results shown in Figs. 3 and 4 for various theoretical scenarios and for short-baseline neutrino oscillation experiments.

##### A. Implications for theoretical scenarios

Apart from the LSND indications, there are (older) hints of neutrino oscillations from the solar neutrino problem and from the atmospheric neutrino anomaly. These additional data have been recently analyzed, within the same three-flavor framework adopted in this work, in [32] for solar neutrinos and in [33] for atmospheric neutrinos.

The results obtained in this work and in [32,33] indicate that the LSND and atmospheric data are difficult to reconcile at 90% C.L. if the subdominant neutrino mass difference is called to solve the solar neutrino problem [32]. In fact, from the LSND analysis (Figs. 3 and 4) we derive  $m^2 \gtrsim 0.22$  eV<sup>2</sup>, while from the atmospheric neutrino analysis [33] we derive the incompatible bound  $m^2 \lesssim 0.1$  eV<sup>2</sup>. These data could be marginally reconciled only by dropping the information provided by the multi-GeV event sample of the Kamiokande experiment, as observed in [24] (see also [29]). If no data are excluded, however, one cannot achieve with three-flavor oscillations a good fit of the solar, atmospheric, and LSND data *at the same time*. The addition of a fourth, sterile neutrino might reconcile all the data without exclusions (see, e.g., [27]), but we think that more robust experimental checks must be performed before adopting such an extreme interpretation.

Let us consider now the interplay between the LSND and the solar neutrino data. As shown in Fig. 4, at any given  $m^2$  there are two regions allowed at 90% C.L. at small and large  $\phi$ . However, only the small  $\phi$  region survives the comparison with solar neutrino data [32], since at large  $\phi$  the solar neutrino deficit becomes almost energy-independent, contrary to the present experimental evidence [34]. The small  $\phi$ , large  $\psi$  allowed solution of Fig. 4 would

indicate that the “lone” neutrino state  $\nu_3$  is dominantly a  $\nu_\mu$ , thus excluding a simultaneous hierarchy of masses and mixings.

Many semi-quantitative three-flavor analyses of laboratory neutrino data cornered a third, marginal “90% LSND allowed region” at small values of  $\phi$  and  $\psi$  [20,23,25,26,30], corresponding to  $\nu_3$  dominantly coupled with  $\nu_\tau$ . This possibility is appealing since small mixings are generally regarded as more natural. However, our quantitative analysis shows that such region does not appear at 90% C.L. for any value  $m^2$  and, therefore, it is unlikely that the  $\nu_\tau$  is the dominant flavor component of  $\nu_3$ .

The threefold maximal mixing scenario (see, e.g., [35]), corresponding to  $(\tan^2 \psi, \tan^2 \phi) = (1, 1/2)$ , is excluded at more than 99% C.L. for all values of  $m^2$  in the LSND sensitivity range, as can be seen in Fig. 4. The quasi-maximal mixing scenario proposed in [28], corresponding to  $\psi \simeq \pi/4$  and small  $\phi$ , also appears to be strongly disfavored by our analysis.

In conclusion, if one believes in the indications from solar *and* LSND neutrino experiments, then the dominant flavor component of the mass eigenstate  $\nu_3$  is the muon neutrino. This conclusion is relevant for model building. The precise bounds on the  $\nu_3$  flavor content can be derived from Fig. 4 at any given value of  $m^2$ , taking into account that the “large  $\phi$ ” solution is excluded by the analysis of solar neutrino data [32].

## B. Implications for short-baseline experiments

The implications of the LSND results for experiments probing the same oscillation channel ( $\nu_\mu \leftrightarrow \nu_e$ ) are straightforward: they should observe a positive indication for neutrino oscillation, or disprove it, if they reach (at least) the LSND sensitivity. This goal should be reached by the KARMEN experiment in about two years [9]. We mention in passing that the NOMAD experiment is also sensitive to  $\nu_e$  appearance for  $m^2 \gtrsim 10 \text{ eV}^2$ , where it is expected to improve the existing limits [36].

The implications for experiments probing different oscillation channels are less evident and require a three-flavor language. Here we focus on  $\nu_\mu \leftrightarrow \nu_\tau$  searches, currently being performed by the CHORUS [16] and NOMAD [17] experiments at CERN. Both experiments are expected to release soon the preliminary results of the first two-year run (1994–95), and are scheduled for additional two years of data taking (1996–97) [37]. Two proposals for their upgrade are currently being considered at CERN, namely, the Tracking and Emulsion for Neutrino Oscillation Research (TENOR) [38], and the Neutrino Apparatus with Improved Capabilities (NAUSICAA) [39]. The Cosmologically Significant Mass Oscillation Search (COSMOS) experiment [40] at Fermilab is also planned to probe the  $\nu_\mu \leftrightarrow \nu_\tau$  channel with an expected sensitivity greater than CHORUS and NOMAD but somewhat lower than TENOR or NAUSICAA.

Figure 5 shows the 90% C.L. regions that can be probed by CHORUS or NOMAD (in two years [16,17] and four years [36,37]), COSMOS, and TENOR or NAUSICAA, using the  $(\tan^2 \psi, \tan^2 \phi)$  representation at fixed values of  $m^2$ . Also shown is the region preferred at 90% C.L. by the combination of all available data (including LSND), as taken from Fig. 4. It can be seen that the CHORUS and NOMAD experiments cannot probe, with a two-year statistics, the region preferred by all the data at 90% C.L. (except for a marginal zone

at  $m^2 \simeq 10 \text{ eV}^2$ ), as already noticed in [18]. However, it is interesting to note that two additional years of data taking will make the CHORUS and NOMAD experiments able to probe a fraction of the small  $\phi$ , large  $\psi$  allowed region (see, e.g., the two top panels in Fig. 5). The COSMOS experiment and the TENOR or NAUSICAA projects will not only improve the sensitivity to the small  $\phi$  solution at low  $m^2$ , but could even probe the large  $\phi$  solution at large  $m^2$  (as in the first panel of Fig. 5).

It follows from Fig. 5 that, if an oscillation signal shows up in CHORUS or NOMAD (after a 4-year run) and if the LSND claim is confirmed, then the mixing angles will be tightly constrained in the small  $\phi$ , large  $\psi$  region. Such a solution would be compatible with solar neutrinos [32], but not with atmospheric neutrinos [33]. Conversely, if the CHORUS and NOMAD oscillation searches give negative results, then the present small  $\phi$ , large  $\psi$  solution will be strongly reduced. The proposed COSMOS, TENOR, and NAUSICAA experiment might probe, in part, the additional possibility offered by the large  $\phi$  solution. We conclude that the running and future  $\nu_\mu \leftrightarrow \nu_\tau$  experiments can explore an interesting fraction of the LSND allowed region, and will provide in any case decisive constraints on the neutrino mixing angles.

We finally mention that the  $\nu_e \rightarrow \nu_e$  reactor experiments in construction at Chooz [41] and Palo Verde [42] are planned to improve the existing limits in the range  $10^{-3} \text{ eV}^2 \lesssim m^2 \lesssim 10^{-2} \text{ eV}^2$ . However, they are not expected to improve the available Bugey bounds in the range of  $m^2$  relevant for LSND ( $m^2 \gtrsim 0.22 \text{ eV}^2$ ) and, therefore, should not have enough sensitivity to probe the 90% C.L. regions shown in Fig. 4. More precisely, the Chooz or Palo Verde sensitivity region would appear as a horizontal band in the  $(\tan^2 \psi, \tan^2 \phi)$  plane [18], with an expected width given by  $0.04 \lesssim \tan^2 \phi \lesssim 25$ , which does not overlap with the 90% C.L. allowed regions of Fig. 4.

## V. CONCLUSIONS

We have studied the interplay between the recent LSND indications and the negative results of the established oscillation searches at accelerators (E776, KARMEN, E531, CDHSW) and reactors (Gösgen, Bugey, Krasnoyarsk). A thorough analysis has been performed assuming two-flavor and three-flavor mixing. The region of neutrino oscillation parameters preferred by all the data has been determined. In particular, the three-flavor analysis in the  $(m^2, \psi, \phi)$  space typically favors two solutions, one at small and the other at large  $\phi$ . Only the small  $\phi$  solution is consistent with the solar neutrino data. A small fraction of the small  $\phi$  solution appears to be in the range explorable by the CHORUS and NOMAD experiments (four year run). A larger fraction of this solution, and even a small part of the large  $\phi$  region, could be probed by the COSMOS experiment at Fermilab and (with greater sensitivity) by the TENOR or NAUSICAA experiments at CERN. Finally, it has been shown (Appendix A) how different statistical treatments of the published LSND data affect the bounds on the neutrino oscillation parameters.



## ACKNOWLEDGMENTS

We acknowledge useful discussions with L. DiLella, U. Dore, J. Ellis, and P. Strolin. We thank the organizers of the CERN Joint Neutrino Meeting of the CHORUS and NOMAD Collaboration, where preliminary results of this work were presented. One of us (G.S.) would like to thank the CERN Particle Physics Experiments Division and the CHORUS Collaboration for kind hospitality during completion of this work, and the INFN for partial support. This work was performed under the auspices of the Theoretical and Astroparticle Network (TAN) of the E.E.C.

## APPENDIX A: REANALYSIS OF THE LSND DATA

The Liquid Scintillator Neutrino Detector (LSND) experiment [1] searches for  $\bar{\nu}_e$  appearance in a  $\bar{\nu}_\mu$  beam from the decay (at rest)

$$\begin{aligned} \pi^+ &\rightarrow \mu^+ + \nu_\mu \\ &\hookrightarrow e^+ + \nu_e + \bar{\nu}_\mu , \end{aligned} \tag{A1}$$

through the reaction

$$\bar{\nu}_e + p \rightarrow e^+ + n . \tag{A2}$$

The maximum  $\bar{\nu}_\mu$  energy is  $E_\nu^{\max} = 52.8$  MeV. For any candidate positron, the LSND detector can determine both its energy  $E_e$  and its vertex coordinate  $L$  (equal to the neutrino path length). The detector covers the range  $L = 29.8 \pm 3.8$  m.

Positron-like events have been observed [2,3] in excess of the estimated background. If this excess is interpreted as a signal of neutrino oscillations, a region of (two-flavor) neutrino mass and mixing parameters appears to be preferred by the data analysis, as shown in Fig. 31 of [2].

In this Appendix we describe how such region can be reproduced to a good accuracy by reanalyzing the published LSND data, and how it gets modified by changing some assumptions. We fix the terminology in Sec. A1, develop the standard analysis in Sec. A2, and discuss variations of the standard analysis in Sec. A3.

### 1. Basic definitions

The total LSND signal  $S$  is defined as the sum of the total (beam-off plus beam-related) background  $B$  and of the event excess  $E$  due to possible oscillations,

$$S = B + E . \tag{A3}$$

The subscript “exp” and “theo” will be used to distinguish the observed values of  $S$  and  $E$  from the theoretical estimates, respectively. No subscript is attached to  $B$ , which is always a simulated quantity.

For a given experimental distribution of the signal (divided in  $N$  bins),  $\{n_i\}_{i=1\dots N}$ , and the associated theoretical distribution  $\{\mu_i\}_{i=1\dots N}$ , a likelihood function  $\mathcal{L}$  can be defined as

$$\mathcal{L} = \prod_{i=1}^N \frac{1}{n_i!} \mu_i^{n_i} e^{-\mu_i} . \quad (\text{A4})$$

The analysis performed by the LSND collaboration [2] is essentially based on the likelihood  $\mathcal{L}_{EL}$  associated to the (experimental and theoretical) double differential distribution  $d^2S/dE_e dL$ ,

$$\mathcal{L}_{EL} = \mathcal{L}(d^2S/dE_e dL) , \quad (\text{A5})$$

having divided the positron energy range ( $20 \text{ MeV} \leq E_e \leq 60 \text{ MeV}$ ) into 20 bins and the length range ( $26.0 \text{ m} \leq L \leq 33.6 \text{ m}$ ) into 38 bins.<sup>2</sup>

Unfortunately, the double differential distributions  $d^2S_X/dE_e dL$  ( $X = \text{exp, theo}$ ) are not published in Refs. [1,2], so that the likelihood function in Eq. (A5) cannot be reproduced exactly. However, one can recover at least the projected distributions  $dS_X/dE_e$  and  $dS_X/dL$  ( $X = \text{exp, theo}$ ) from [1,2] and thus calculate the corresponding likelihoods  $\mathcal{L}_E$  and  $\mathcal{L}_L$ . In the absence of more detailed information, we assume that the total likelihood is factorizable,

$$\begin{aligned} \mathcal{L}_{EL} &\sim \mathcal{L}_E \times \mathcal{L}_L \\ &= \mathcal{L}(dS/dE_e) \times \mathcal{L}(dS/dL) , \end{aligned} \quad (\text{A6})$$

as if  $dS/dE_e$  and  $dS/dL$  were independent. Although such statistical independence is never exactly realized, we will see *a posteriori* that the published LSND oscillation analysis [2] is reproduced rather well through the approximation Eq. (A6).

In the next subsection we discuss how the relevant distributions of the signal can be recovered from Refs. [1,2] and then used to perform a maximum likelihood analysis.

## 2. Standard Analysis

The approximate likelihood function in Eq. (A6) is based on the four distributions  $dS_{\text{exp}}/dE_e$ ,  $dS_{\text{exp}}/dL$ ,  $dS_{\text{theo}}/dE_e$ , and  $dS_{\text{theo}}/dL$ . The first two can be read off Fig. 30(a) and 30(d) of [2] respectively (dots with statistical error bars). The last two are estimated as follows.

The double differential (theoretical) distribution of events  $E$  in excess of the background is calculated as

$$\frac{d^2E_{\text{theo}}}{dE_e dL} = \mathcal{N} \int dE'_e \frac{d\Phi_\nu}{dE_\nu} L^{-2} \sigma(E_\nu) \varepsilon(E'_e) R(E_e, E'_e) P(L/E_\nu) , \quad (\text{A7})$$

---

<sup>2</sup>Actually, the complete LSND analysis [2] includes also subdominant information related to the positron scattering angle and the event pattern recognition.

where  $E'_e$  and  $E_e$  are the *true* and *measured* positron energy respectively,  $E_\nu$  is the neutrino energy,  $d\Phi_\nu/dE_\nu$  is the neutrino energy spectrum,  $\sigma$  is the neutrino cross section,  $\varepsilon$  is the detector efficiency,  $R$  is the resolution function,  $P$  is the oscillation probability, and  $\mathcal{N}$  is a normalization factor.

The Michel energy spectrum  $d\Phi_\nu/dE_\nu$  of  $\bar{\nu}_\mu$ 's from  $\mu^+$  decay at rest is well known (see, e.g., Fig. 6 in [1]). The total flux varies approximately with the inverse square of the distance  $L$  (see Sec. II B of [2]).

The neutrino cross section  $\sigma$  for the reaction (A2) is also well known [43]. The neutrino energy and the (true) positron energy  $E'_e$  are tightly related,  $E_\nu = E'_e + 1.8 \text{ MeV} + \delta(\theta_e)$ , where  $\delta$  is a small (and often neglected) kinematical correction depending on the positron scattering angle  $\theta_e$ . We have applied a fixed correction corresponding to the average scattering angle  $\cos\theta_e \simeq 0.2$  (see Sec. VI C of [2]).

The efficiency  $\varepsilon(E'_e)$  for detecting a positron with true energy  $E'_e$  can be recovered from Fig. 9 in [2]. It varies from 40% to 90% above the analysis threshold ( $E_e \geq 20 \text{ MeV}$ ).

The difference between the measured and true positron energy is well approximated by a Gaussian energy resolution function  $R(E_e, E'_e)$  with one-sigma width equal to 7.7% at 52.8 MeV, and scaling as  $1/E'_e$  for other energies (see Sec. VI D of [1]).

Finally, the normalization factor  $\mathcal{N}$  is fixed by imposing that for 100% transmutation ( $P = 1$ ) the event excess  $E_{\text{theo}}$  (integrated over the detector length and over the energy range  $20 \text{ MeV} \leq E_e \leq 60 \text{ MeV}$ ) be equal to 16670 events, as reported in Table IV of [2].

We have checked that, for  $P = 1$ , the shape of  $dE_{\text{theo}}/dE_e$  derived from Eq. (A7) compares very well with the corresponding LSND simulation (Fig. 7 in [2]). Moreover, our estimated value of  $E_{\text{theo}}$ , integrated over the energy subrange  $36 \text{ MeV} \leq E_e \leq 60 \text{ MeV}$ , coincides with the LSND quoted value (12500 events, see Table III of [2]) within 0.5%. These two nontrivial checks add confidence in our calculation of the event excess due to neutrino oscillations through Eq. (A7).

Concerning the background  $B$ , the relevant distributions  $dB/dE_e$  and  $dB/dL$  are not reported explicitly in the LSND publications [1,2]. We have derived them indirectly by subtraction,  $B = S - E$ . More precisely, Figs. 30(a) and 30(d) in [2] show (as solid lines) the distributions  $dS_{\text{theo}}/dE$  and  $dS_{\text{theo}}/dL$  of the signal expected for the oscillation case  $(\Delta m_\nu^2, \sin^2 2\theta) = (19 \text{ eV}^2, 0.006)$ . We calculate  $dE_{\text{theo}}/dE$  and  $dE_{\text{theo}}/dL$  from Eq. (A7) for the same oscillation parameters and then obtain the background distributions by subtraction,  $dB = dS_{\text{theo}} - dE_{\text{theo}}$ .

Figs. 6 and 7 show, respectively, the distributions  $dB/dE_e$  and  $dB/dL$  derived in this way (dashed histograms). The integrated background is  $B = 1701$  events. To guide the eye, we also show in Figs. 6 and 7 the corresponding distributions of  $S_{\text{exp}}$  (dots with error bars) and of  $S_{\text{theo}}$  [for  $(m^2, \sin^2 2\theta) = (19 \text{ eV}^2, 0.006)$ ], as taken from Figs. 30(a) and 30(d) of [2] respectively. The integrated signal is  $S_{\text{exp}} = 1763$  events, corresponding to  $S_{\text{exp}} - B = 62$  excess events.

With the above ingredients we calculate, for a given oscillation probability function  $P$ , the  $E$  and  $L$  distributions of the expected signal  $S_{\text{theo}}$  and the associated likelihood [Eq. (A6)], from which the confidence contours of Fig. 1 have been obtained.

When used in combination with other neutrino oscillation data, the LSND likelihood is transformed in a  $\chi^2$  through the relation [6]  $\chi^2 = -\ln \mathcal{L}/2$ .

### 3. Variations in the analysis

The “standard” analysis of the LSND data described in the previous section (and used throughout this work) makes use of the  $E_e$  and  $L$  distributions of the data (Figs. 6 and 7) through a maximum likelihood analysis.

In order to test the stability of the “standard” LSND limits shown in Fig. 1, we have performed a few alternative analyses of the LSND data that gradually deviate from the standard one. The results are shown in Fig. 8.

Fig. 8(a) shows the 90 and 99 % C.L. limits obtained by dropping the likelihood factor  $\mathcal{L}_L$  in Eq. (A6). The limits are only slightly relaxed with respect to Fig. 1. In fact, the fit is basically driven by the excess of events in a few bins of the energy distribution (Fig. 6), while the path length distribution (Fig. 7) is not really discriminating within the statistical error bars. For the sake of simplicity, only the dominant  $E_e$  distribution is used in all panels of Fig. 8.

Fig. 8(b) shows the LSND limits from a “true”  $\chi^2$  analysis of the  $E_e$  distribution (i.e., the canonical definition of  $\chi^2$  is used and not  $-\ln \mathcal{L}/2$ ). Only statistical errors are included. A comparison with Fig. 8(a) shows a slight relaxation of the C.L. contours for small mixing (i.e., for lower rates), as expected from the Gaussian approximation of a Poisson distribution which is implied by the  $\chi^2$  method.

Fig. 8(c) shows the results of the same  $\chi^2$  analysis of Fig. 8(b) with the addition of a plausible 10% uncertainty in the background normalization [2]. The correlation of this error between any two bins is taken equal to 1. The LSND oscillation limits are somewhat relaxed, and the data became even compatible with no oscillations at about 99% C.L.

In Fig. 8(d) the same analysis of Fig. 8(c) is repeated by dividing the energy distribution in 5 bins instead of 20. The rationale for this exercise is the erratic position of bins where there is a significant event excess (see Fig. 6), that might be a symptom of statistical fluctuations. Such fluctuations should be somewhat flattened by grouping bins. In fact, the LSND limits appear to be slightly relaxed as compared with Fig. 8(c). A more evident effect is obtained by dividing the  $E_e$  distribution in just two bins, as shown in Fig 8(e).

Finally, Fig. 8(f) shows the LSND limits obtained when the  $E_e$  distribution is fully integrated, i.e., when only the total number of events is used. Since the total event excess (62 events) is smaller than the systematic uncertainty of the background (10% of 1701 events), no significant indication in favor of neutrino oscillations is obtained, and the analysis gives only *exclusion* contours. Therefore, the preference for nonzero values of the neutrino oscillation parameters in Figs.8(a)–(e) appears to be driven by the information contained in the positron energy spectrum.

In conclusion, the exercises described in this section show that, as far as the published information is used, the “standard” LSND limits of Fig. 1 appear to be dominated by the detailed energy distribution of the observed event excess. Different ways of treating this distribution may lead to significant changes in the C.L. contours. In particular, the indications in favor of neutrino oscillations are increasingly weakened by gradually integrating the energy spectrum information.

## APPENDIX B: REANALYSIS OF THE KARMEN DATA

The Karlsruhe Rutherford Medium Energy Neutrino (KARMEN) experiment [8–10] is being performed at the pulsed spallation neutron facility ISIS of the Rutherford Appleton Laboratory. A search is made for  $\nu_e$  and  $\bar{\nu}_e$  appearance from  $\nu_\mu$  and  $\bar{\nu}_\mu$  produced in  $\pi^+$  and  $\mu^+$  decay at rest. Therefore, the energy spectrum of the neutrino source,  $d\Phi_\nu/dE$ , is the same as in the LSND experiment. The KARMEN detector, a 56 ton liquid scintillation calorimeter, is located at a distance  $L = 17.5 \pm 1.75$  m (front-end range) from the source. The pulsed time structure of the beam can be exploited to achieve a strong suppression of the background.

At present, the number of candidate events is consistent with the estimated background for both oscillation channels,  $\bar{\nu}_\mu \leftrightarrow \bar{\nu}_e$  and  $\nu_\mu \leftrightarrow \nu_e$ . These negative results can be used to constrain the neutrino mass and mixing parameters. Our statistical analysis of the constraints for the two oscillation channels and their combination is detailed below.

### 1. Channel $\bar{\nu}_\mu \leftrightarrow \bar{\nu}_e$

For this channel we use three basic inputs [9]: (1) the number of events (prompt positrons) observed in excess of the expected background,  $N_{\text{exp}} \pm \sigma_N = -0.4_{-5.3}^{+6.9}$ ; (2) the number of events expected for 100% transmutation,  $N_{\text{max}} = 3038$ ; and (3) the positron energy spectrum  $S(E_{e^+})$  (Fig. 6 of [10]) expected for 100% transmutation. The above inputs refer to the default energy window  $20 \leq E_{e^+} \leq 52$  MeV. The approximate energy relation  $E_{\bar{\nu}_e} \simeq E_{e^+} + 1.8$  MeV is adopted.

The expected (theoretical) number of positrons for a generic oscillation probability  $P = P(L/E_{\bar{\nu}_e})$  is then given by

$$N_{\text{theo}} = N_{\text{max}} \frac{\int_{L-D/2}^{L+D/2} dL L^{-2} \int dE_{e^+} S(E_{e^+}) P(L/E_{\bar{\nu}_e})}{\int_{L-D/2}^{L+D/2} dL L^{-2} \int dE_{e^+} S(E_{e^+})}, \quad (\text{B1})$$

where  $D$  is the detector length (3.5 m).

The probability  $\epsilon$  that a difference as large as  $\Delta = (N_{\text{theo}} - N_{\text{exp}})/\sigma_N$  be a statistical fluctuation is obtained by integrating a one-sided Gaussian ( $N_{\text{theo}}$  being nonnegative),

$$1 - \epsilon = \sqrt{\frac{2}{\pi}} \int_0^\Delta dx \exp(-x^2/2). \quad (\text{B2})$$

As a check, we draw in Fig. 9 the exclusion curve (dotted line) corresponding to  $1 - \epsilon = 90\%$  in the usual two-flavor mass-mixing plane. This curve matches well the 90% C.L. contour reported by the KARMEN collaboration in [9] for the same oscillation channel.

When a combination with other oscillation data is performed in a global  $\chi^2$  analysis, we use a “fake”  $\chi^2$  statistic determined by probability inversion [ $\chi^2 = \chi^2(\epsilon)$ ], yielding for any assigned C.L. the same exclusion curves.

## 2. Channel $\nu_\mu \leftrightarrow \nu_e$

In this channel the energy spectrum is monochromatic ( $E_{\nu_\mu} = 29.8$  MeV). We use three basic inputs [9]: (1) the number of candidate events,  $N = 1$ ; (2) the estimated background  $N_B$  and its 1-sigma uncertainty,  $N_B \pm \sigma_B = 2 \pm 0.3$ ; and (3) the number of events expected for 100% transmutation,  $N_{\max} = 154$ .

For a generic oscillation probability, the expected number of events is then calculated as

$$N_{\text{theo}} = N_{\max} \frac{\int_{L-D/2}^{L+D/2} dL L^{-2} P(L/E_{\nu_\mu})}{\int_{L-D/2}^{L+D/2} dL L^{-2}}. \quad (\text{B3})$$

The confidence level  $1 - \epsilon$  associated to  $N_{\text{theo}}$  can be calculated by using the statistics appropriate to a Poisson process with background [6], with an allowance for statistical fluctuations of the background itself [44]:

$$1 - \epsilon = 1 - \frac{\int_0^\infty dn_B f(n_B) e^{-(n_B + N_{\text{theo}})} \sum_{n=0}^N (n_B + N_{\text{theo}})^n / n!}{\int_0^\infty dn_B f(n_B) e^{-n_B} \sum_{n=0}^N n_B^n / n!}, \quad (\text{B4})$$

where

$$f(n_B) = \frac{1}{\sqrt{2\pi}\sigma_B} \exp\left[-\frac{1}{2} \left(\frac{n_B - N_B}{\sigma_B}\right)^2\right]. \quad (\text{B5})$$

The curve corresponding to  $1 - \epsilon = 90\%$  in the usual mass-mixing plane is shown in Fig. 9 as a thin, solid line. It reproduces in detail the 90% C.L. contour reported by the KARMEN collaboration in [9].

As for the antineutrino channel, we use a “fake”  $\chi^2$  statistic determined by probability inversion [ $\chi^2 = \chi^2(\epsilon)$ ] when a combination with other data is performed. In particular, we combine the two KARMEN oscillation channels,  $\nu_\mu \leftrightarrow \nu_e$  and  $\bar{\nu}_\mu \leftrightarrow \bar{\nu}_e$ , by summing the corresponding  $\chi^2$ 's. The curve corresponding to a variation of 4.61 in the total  $\chi^2$  (90% C.L. for two degrees of freedom) is shown in Fig. 9 as a thick, solid curve (the same curve reported in the top left panel of Fig. 2). It can be seen from a comparison of the three curves in Fig. 9 that the channel  $\bar{\nu}_\mu \leftrightarrow \bar{\nu}_e$  dominates the KARMEN exclusion region.

## REFERENCES

- [1] LSND Collaboration, C. Athanassopoulos *et al.*, Los Alamos Report No. LA-UR-96-1327, nucl-ex/9605002, submitted to Nucl. Instr. Methods.
- [2] LSND Collaboration, C. Athanassopoulos *et al.*, Phys. Rev. C **54**, 2685 (1996).
- [3] LSND Collaboration, C. Athanassopoulos *et al.*, Phys. Rev. Lett. **77**, 3082 (1996).
- [4] LSND Collaboration, C. Athanassopoulos *et al.*, Phys. Rev. Lett. **75**, 2650 (1995).
- [5] J. R. Primack, J. Holtzmann, A. Klypin, and D. O. Caldwell, Phys. Rev. Lett. **74**, 2160 (1995).
- [6] Review of Particle Physics, R. M. Barnett *et al.*, Phys. Rev. D **54**, 1 (1996).
- [7] E776 Collaboration, L. Borodovsky *et al.*, Phys. Rev. Lett. **68**, 274 (1992).
- [8] KARMEN Collaboration, J. Kleinfeller *et al.*, in *TAUP '95*, Proceedings of the Fourth International Workshop on Theoretical and Phenomenological Aspects of Underground Physics, Toledo, Spain, 1995, edited by A. Morales, J. Morales, and J. A. Villar [Nucl. Phys. B (Proc. Suppl.) **48**, 207 (1995)].
- [9] KARMEN Collaboration, J. Kleinfeller *et al.*, in *Neutrino '96*, 17th International Conference on Neutrino Physics and Astrophysics, Helsinki, Finland, 1996, to appear in the Proceedings.
- [10] KARMEN Collaboration, K. Eitel *et al.*, in the *Proceedings of the 7th International Workshop on Neutrino Telescopes*, Venice, Italy, 1996, edited by M. Baldo-Ceolin (University of Padova, Italy, 1996), p. 119.
- [11] G. Zacek *et al.*, Phys. Rev. D **34**, 2621 (1986).
- [12] B. Achkar *et al.*, Nucl. Phys. B **434**, 503 (1995).
- [13] G. S. Vidyakin *et al.*, Pis'ma Zh. Eksp. Teor. Fiz. **59**, 364 (1994) [JETP Lett. **59**, 390 (1994)].
- [14] CDHSW Collaboration, F. Dydak *et al.*, Phys. Lett. B **134**, 281 (1984).
- [15] E531 Collaboration, N. Ushida *et al.*, Phys. Rev. Lett. **57**, 2897 (1986).
- [16] CHORUS Collaboration, D. Macina *et al.*, in *TAUP '95* [8], p. 183; D. Saltzberg *et al.*, in *Neutrino Telescopes '96* [10], p. 91.
- [17] NOMAD Collaboration, M. Laveder *et al.*, in *TAUP '95* [8] p. 188; A. Rubbia *et al.*, in *Neutrino Telescopes '96* [10], p. 101.
- [18] G. L. Fogli, E. Lisi, and G. Scioscia, Phys. Rev. D **52**, 5334 (1995).
- [19] G. L. Fogli, E. Lisi, and D. Montanino, Phys. Rev. D **49**, 3626 (1994); Astropart. Phys. **4**, 177 (1995).
- [20] H. Minakata, Phys. Lett. B **356**, 61 (1995).
- [21] S. M. Bilenky, A. Bottino, C. Giunti, and C. W. Kim, Phys. Lett. B **356**, 273 (1995); Phys. Rev. D **54**, 1881 (1996).
- [22] S. M. Bilenky, C. Giunti, C. W. Kim, and S. T. Petcov, Phys. Rev. D **54**, 4432 (1996).
- [23] K. S. Babu, J. C. Pati, and F. Wilczek, Phys. Lett. B **359**, 351 (1995); **364**, 251(E) (1995).
- [24] C. Y. Cardall and G. M. Fuller, Phys. Rev. D **53**, 4421 (1996).
- [25] M. Tanimoto, Phys. Rev. D **53**, 6632 (1996).
- [26] K. Kang, J. E. Kim, and P. Ko, Z. Phys. C **72**, 671 (1996).
- [27] S. Goswami, Calcutta University Report No. CUPP-95-4, hep-ph/9507212, to be published in Phys. Rev. D.

- [28] E. Torrente-Lujan, Phys. Lett. B **389**, 557 (1996).
- [29] O. Yasuda and H. Minakata, Tokyo Metropolitan University Report No. TMUP-HEL-9604, hep-ph/9602386 (unpublished).
- [30] A. Acker and S. Pakvasa, Hawaii University Report, hep-ph/9611423 (unpublished).
- [31] It has been observed recently (Ref. [6], p. 298) that the published number of expected  $\nu_e$  charged current events in the E531 experiment [15] must be corrected by a factor of  $\sim 0.48$  in the analysis of the  $\nu_e \leftrightarrow \nu_\tau$  channel. As a consequence, the corresponding bounds on the mixing angle become weaker (by a factor of about two). We have applied this correction factor in the present analysis. The correction was not known at the time of our previous work [18]. However, the constraint from the E531 experiment in the  $\nu_e \leftrightarrow \nu_\tau$  are never dominant in the analysis, and we have checked that the results of our previous global fit shown in Fig. 10 of [18] are negligibly altered by such correction.
- [32] G. L. Fogli, E. Lisi, and D. Montanino, Phys. Rev. D **54**, 2048 (1996).
- [33] G. L. Fogli, E. Lisi, D. Montanino, and G. Scioscia, Institute for Advanced Study Report No. IASSNS-AST-96-41, hep-ph/9607251, to appear in Phys. Rev. D.
- [34] P. I. Krastev and S. T. Petcov, Institute for Advanced Study Report No. IASSNS-AST-96-58, hep-ph/9612243 (unpublished).
- [35] P. F. Harrison, D. H. Perkins, and W. G. Scott, Phys. Lett. B **349**, 137 (1995); Rutherford Appleton Laboratory Report No. RAL-TR-97-009, hep-ph/9702243, to appear in Phys. Lett. B.
- [36] L. DiLella, seminar at CERN, Jan. 1997.
- [37] P. Strolin, seminar at CERN, Jan. 1997.
- [38] A. Ereditato, G. Romano, and P. Strolin, “*TENOR: A new experiment for the search of  $\nu_\mu$ - $\nu_\tau$  oscillations,*” CHORUS Internal note No. 96-03, 1996 (unpublished).
- [39] J. J. Gomez-Cadenas and J. A. Hernando, Nucl. Instrum. Methods A **381**, 223 (1996).
- [40] COSMOS Collaboration, R. A. Sidwell *et al.*, in *Neutrino '96* [9], to appear in the Proceedings.
- [41] Chooz Collaboration Proposal (unpublished); available at the URL [http://duphy4.physics.drexel.edu/chooz\\_pub/index.html](http://duphy4.physics.drexel.edu/chooz_pub/index.html) .
- [42] Palo Verde Collaboration Proposal (unpublished); available at the URL <http://www.cco.caltech.edu/~songhoon/Palo-Verde/Palo-Verde.html> .
- [43] C. H. Llewellyn Smith, Phys. Rep. **3**, 262 (1972).
- [44] O. Helene, Nucl. Instr. and Methods **212**, 319 (1983).



## FIGURES

FIG. 1. Region of the  $2\nu$  oscillation parameters preferred by the LSND data (our reanalysis) at 68, 90, and 99 % C.L. ( $N_{\text{DF}} = 2$ ).

FIG. 2. Laboratory oscillation data in two flavors (our reanalysis). Left panels: contours of regions excluded at 90 (solid) and 99 % (dashed) C.L. by the accelerator experiments KARMEN and E776, and by reactor experiments (Gösgen, Bugey, and Krasnoyarsk combined). Right panels: variations in the region preferred by the LSND data (see Fig. 1) with the progressive addition of the KARMEN, E776, and reactor data.

FIG. 3. Three-flavor analysis of the most constraining laboratory oscillation experiments (LSND, KARMEN, E776, E531, CDHSW, Gösgen, Bugey, and Krasnoyarsk combined). The preferred region in the  $3\nu$  parameter space ( $m^2, \tan^2 \psi, \tan^2 \phi$ ) is shown through twelve ( $m^2, \tan^2 \phi$ ) sections at fixed, representative values of  $\tan^2 \psi$ . Solid lines: 90% C.L. contours ( $\Delta\chi^2 = 6.25$  for  $N_{\text{DF}} = 3$ ). Dotted lines: 99% C.L. contours ( $\Delta\chi^2 = 11.36$ ).

FIG. 4. As in Fig. 3, but in  $(\tan^2 \phi, \tan^2 \psi)$  sections at twelve representative values of  $m^2$ .

FIG. 5. Regions of the parameter space explorable at 90% C.L. by the following  $\nu_\mu \rightarrow \nu_\tau$  experiments (in order of increasing sensitivity): CHORUS or NOMAD in two years (thick, dotted line) and four years (thin, solid line), COSMOS (dashed line), and TENOR or NAUSICAA (thin, dotted line). These experiments can probe a fraction of the zone preferred at 90% C.L. by the combination of all the available data, including LSND (thick, solid line).

FIG. 6. Energy distribution  $dS/dE_e$  of the LSND signal (20 bins). Dashed line: background component  $dB/dE_e$  (our reanalysis). Solid line: signal  $dS_{\text{theo}}/dE_e$  expected for  $(m^2, \sin^2 2\theta) = (19 \text{ eV}^2, 0.006)$ , as taken from Fig. 30(a) of [2]. Dots with statistical error bars: observed signal  $dS_{\text{exp}}/dE_e$ , from Fig. 30(a) of [2].

FIG. 7. As in Fig. 6, but for the path length distribution  $dS/dL$  of the LSND signal (38 bins).

FIG. 8. Variations in the LSND bounds with respect to the “standard” bounds of Fig. 1, as a result of data analyses different from  $\mathcal{L}_{EL}$  maximization. (a) Maximization of  $\mathcal{L}_E$  only. (b)  $\chi^2$  analysis of the energy distribution of the signal with statistical errors only. (c)  $\chi^2$  analysis of the energy distribution, assuming a systematic 10% uncertainty in the overall background normalization. (d) As in (c), but dividing the energy distribution in 5 bins. (e) As in (c), but dividing the energy distribution in 2 bins. (f) As in (c), but integrating the total signal (= 1 bin). See the text for details.

FIG. 9. Results of our reanalysis of the KARMEN data for the neutrino and antineutrino channels and their combination. Contours are drawn at 90% C.L. ( $\Delta\chi^2 = 4.61$  for  $N_{\text{DF}} = 2$ ).

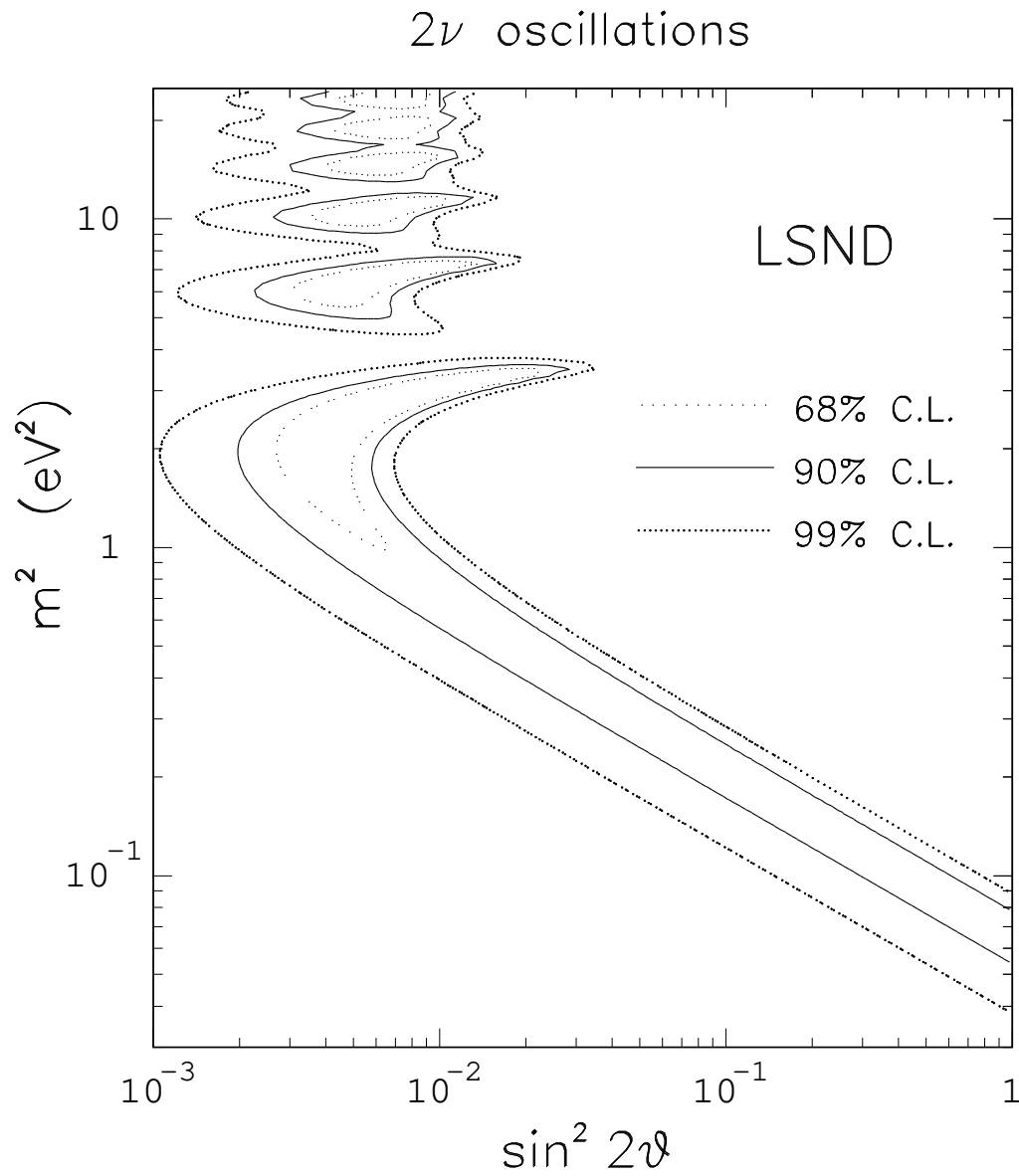


FIG. 1. Region of the  $2\nu$  oscillation parameters preferred by the LSND data (our reanalysis) at 68, 90, and 99 % C.L. ( $N_{\text{DF}} = 2$ ).

## $2\nu$ oscillations

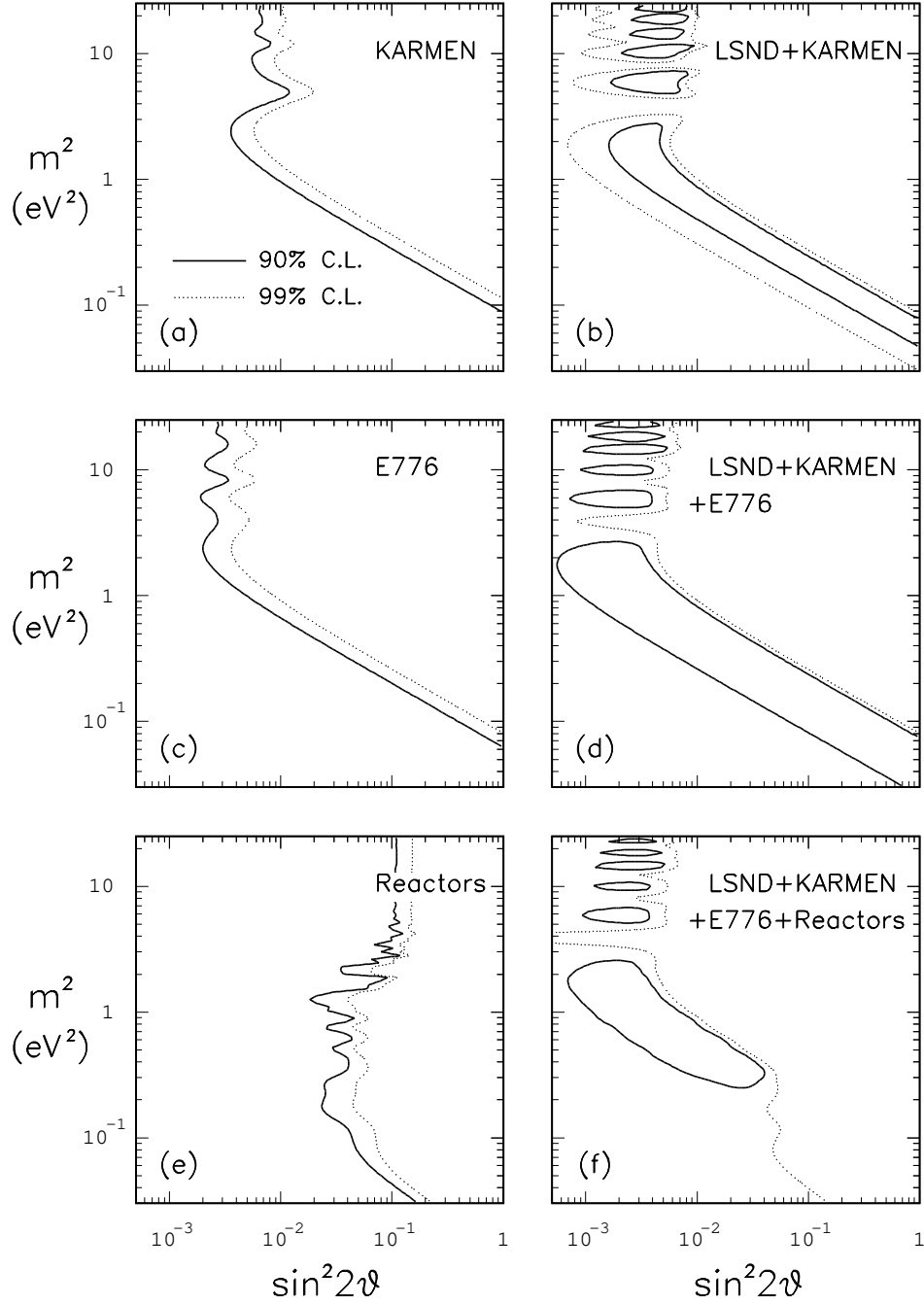


FIG. 2. Laboratory oscillation data in two flavors (our reanalysis). Left panels: contours of regions excluded at 90 (solid) and 99 % (dashed) C.L. by the accelerator experiments KARMEN and E776, and by reactor experiments (Gösgen, Bugey, and Krasnoyarsk combined). Right panels: variations in the region preferred by the LSND data (see Fig. 1) with the progressive addition of the KARMEN, E776, and reactor data.

# $3\nu$ oscillations

LSND + KARMEN + E776 + E531 + CDHSW + Goesgen + Bugey + Krasnoyarsk

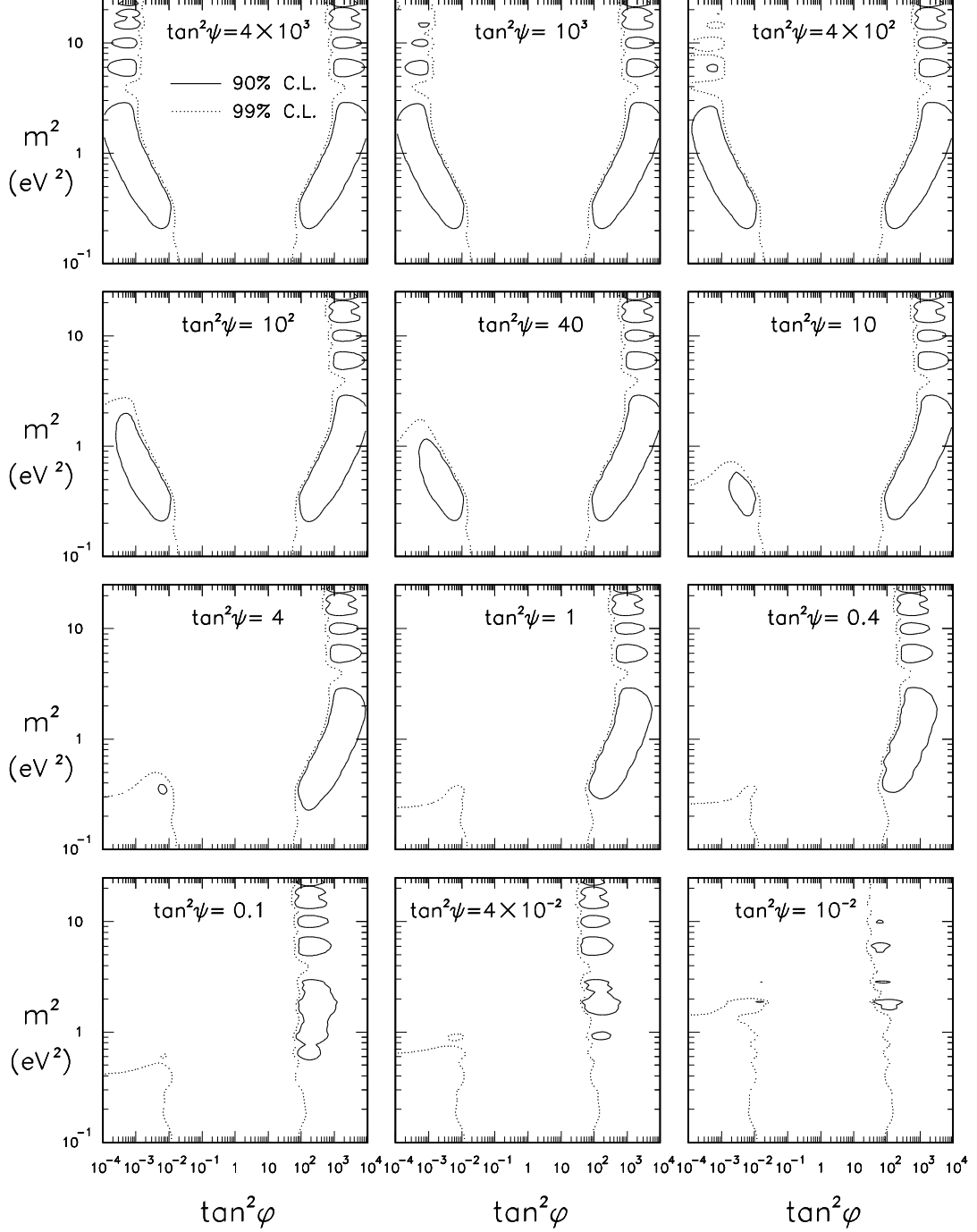


FIG. 3. Three-flavor analysis of the most constraining laboratory oscillation experiments (LSND, KARMEN, E776, E531, CDHSW, Gösgen, Bugey, and Krasnoyarsk combined). The preferred region in the  $3\nu$  parameter space ( $m^2$ ,  $\tan^2 \psi$ ,  $\tan^2 \phi$ ) is shown through twelve ( $m^2$ ,  $\tan^2 \phi$ ) sections at fixed, representative values of  $\tan^2 \psi$ . Solid lines: 90% C.L. contours ( $\Delta\chi^2 = 6.25$  for  $N_{\text{DF}} = 3$ ). Dotted lines: 99% C.L. contours ( $\Delta\chi^2 = 11.36$ ).

# $3\nu$ oscillations

LSND + KARMEN + E776 + E531 + CDHSW + Goesgen + Bugey + Krasnoyarsk

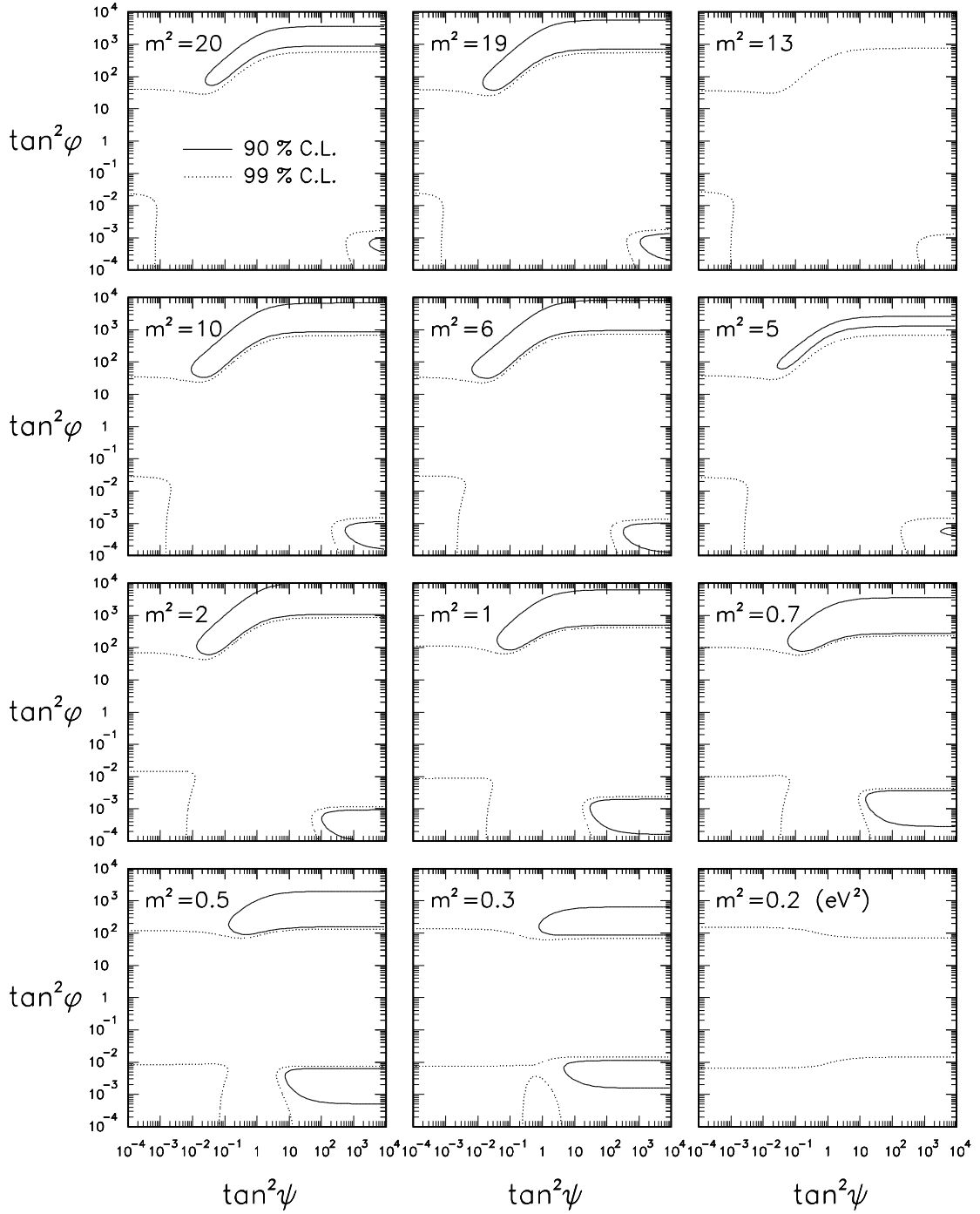


FIG. 4. As in Fig. 3, but in  $(\tan^2 \phi, \tan^2 \psi)$  sections at twelve representative values of  $m^2$ .

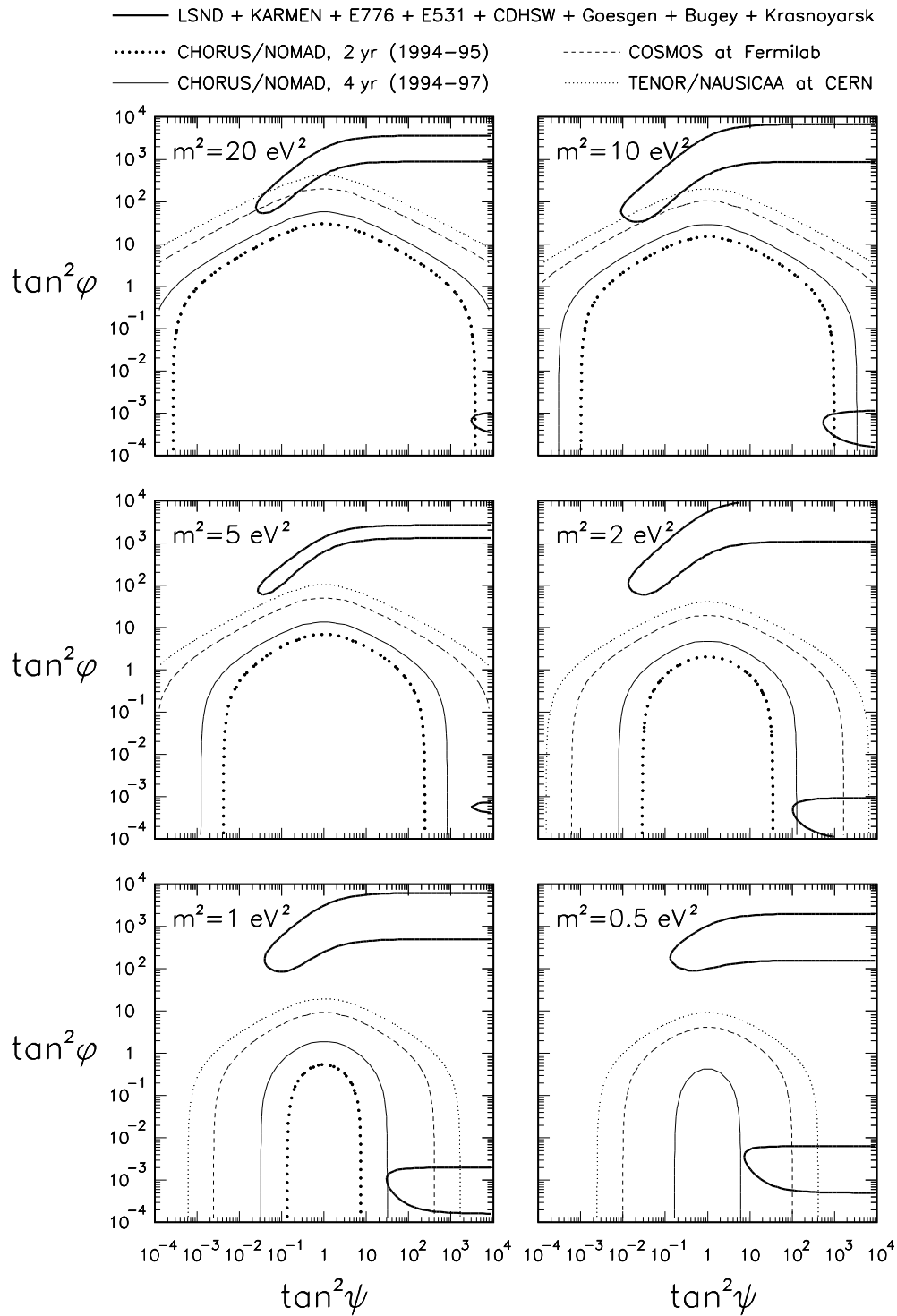


FIG. 5. Regions of the parameter space explorable at 90% C.L. by the following  $\nu_\mu \rightarrow \nu_\tau$  experiments (in order of increasing sensitivity): CHORUS or NOMAD in two years (thick, dotted line) and four years (thin, solid line), COSMOS (dashed line), and TENOR or NAUSICAA (thin, dotted line). These experiments can probe a fraction of the zone preferred at 90% C.L. by the combination of all the available data, including LSND (thick, solid line).

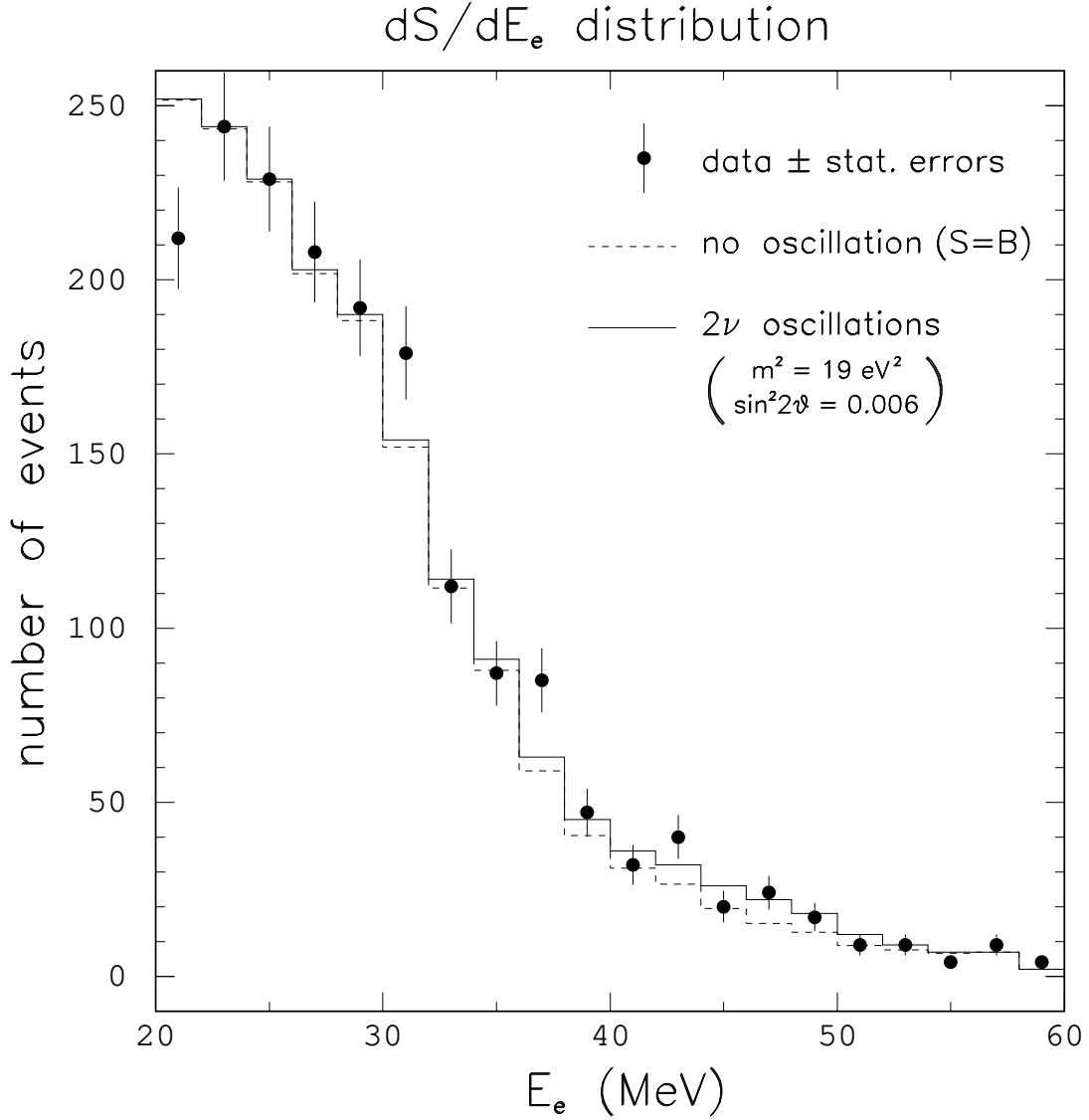


FIG. 6. Energy distribution  $dS/dE_e$  of the LSND signal (20 bins). Dashed line: background component  $dB/dE_e$  (our reanalysis). Solid line: signal  $dS_{\text{theo}}/dE_e$  expected for  $(m^2, \sin^2 2\theta) = (19 \text{ eV}^2, 0.006)$ , as taken from Fig. 30(a) of [2]. Dots with statistical error bars: observed signal  $dS_{\text{exp}}/dE_e$ , from Fig. 30(a) of [2].

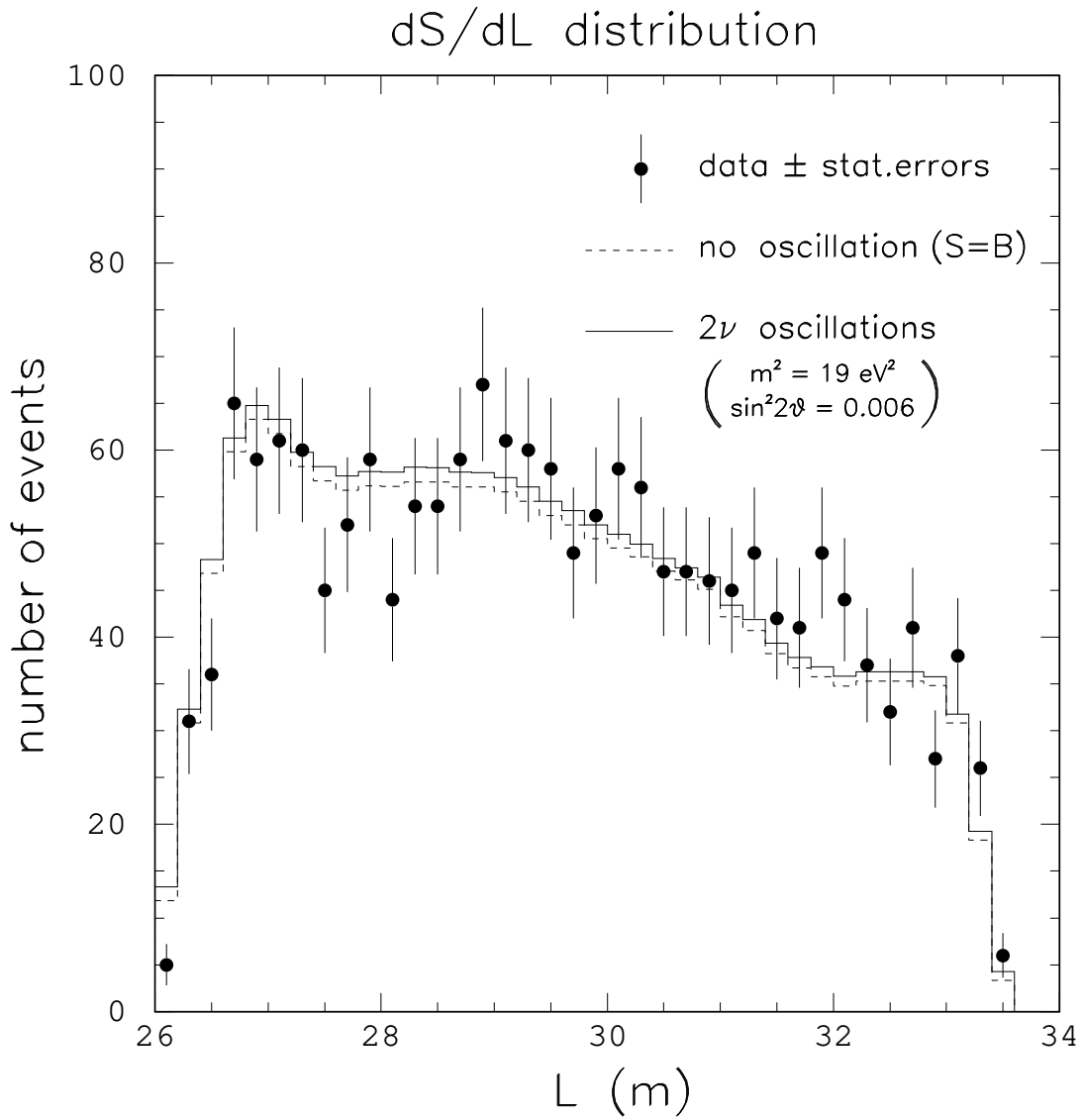


FIG. 7. As in Fig. 6, but for the path length distribution  $dS/dL$  of the LSND signal (38 bins).



Different  $2\nu$  analyses of the  $E_e$  distribution (LSND)

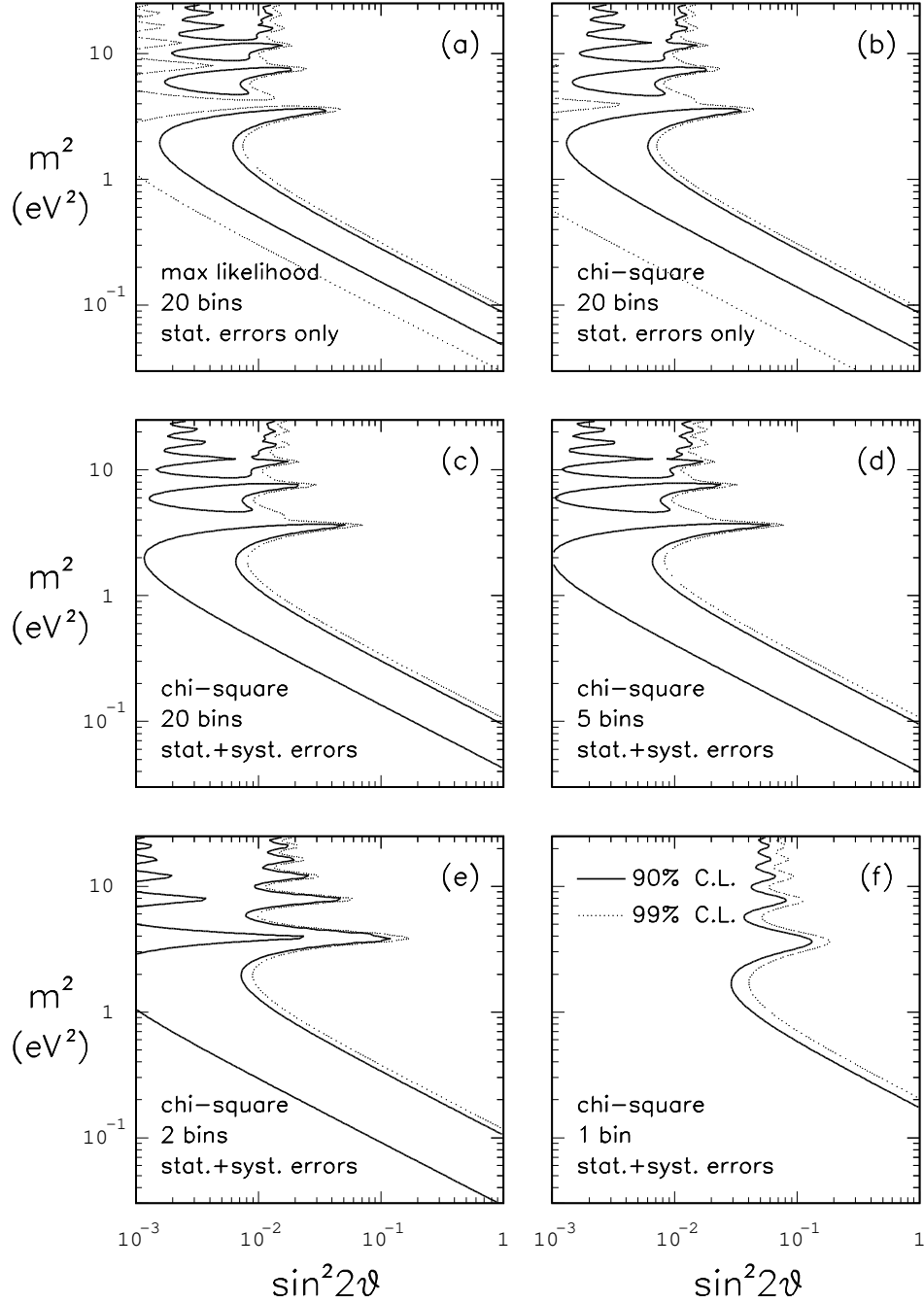


FIG. 8. Variations in the LSND bounds with respect to the “standard” bounds of Fig. 1, as a result of of data analyses different from  $\mathcal{L}_{EL}$  maximization. (a) Maximization of  $\mathcal{L}_E$  only. (b)  $\chi^2$  analysis of the energy distribution of the signal with statistical errors only. (c)  $\chi^2$  analysis of the energy distribution, assuming a systematic 10% uncertainty in the overall background normalization. (d) As in (c), but dividing the energy distribution in 5 bins. (e) As in (c), but dividing the energy distribution in 2 bins. (f) As in (c), but integrating the total signal (= 1 bin). See the text for details.

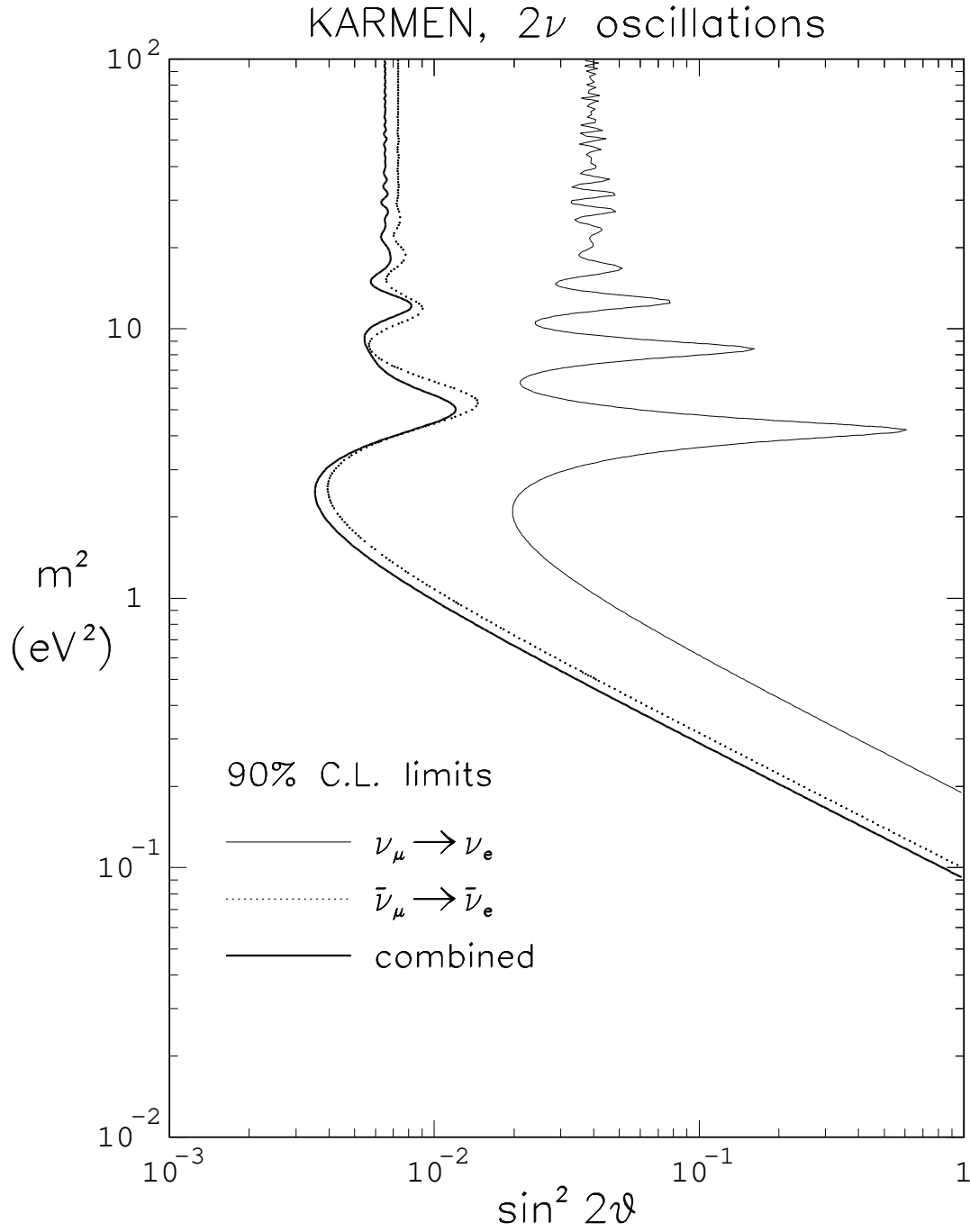


FIG. 9. Results of our reanalysis of the KARMEN data for the neutrino and antineutrino channels and their combination. Contours are drawn at 90% C.L. ( $\Delta\chi^2 = 4.61$  for  $N_{\text{DF}} = 2$ ).